nature photonics

REVIEW ARTICLE

https://doi.org/10.1038/s41566-021-00836-5

Advances in Brillouin–Mandelstam light-scattering spectroscopy

Fariborz Kargar ✉ and Alexander A. Balandin

Recent years have witnessed a much broader use of Brillouin inelastic light-scattering spectroscopy for the investigation of phonons and magnons in novel materials, nanostructures and devices. Driven by the developments in instrumentation and the strong need for accurate knowledge on the energies of elemental excitations, Brillouin–Mandelstam spectroscopy is rapidly becoming an essential technique that is complementary to Raman inelastic light-scattering spectroscopy. We provide an overview of recent progress in the Brillouin light-scattering technique, focusing on the use of this photonic method for the investigation of confined acoustic phonons, phononic metamaterials and magnon propagation and scattering. This Review emphasizes the emerging applications of Brillouin–Mandelstam spectroscopy for phonon-engineered structures and spintronic devices, and concludes with a perspective on future directions.

Brillouin light-scattering (BLS) spectroscopy, also referred to as Brillouin–Mandelstam light-scattering (BMS) spectroscopy, is the inelastic scattering of light by thermally generated or coherently excited elemental excitations such as phonons or magnons. In the early decades of the 1900s[1–3], the French and the Russian scientists Leon Brillouin and Leonid Mandelstam independently predicted interactions between light and thermally excited phonons in solids. Mandelstam, together with his associate Grigory Landsberg, went on to study light scattering on thermal excitations experimentally in quartz crystals, but succeeded in recording the scattering from optical phonons. The fascinating story of these efforts, independent from those of Raman and Krishnan who experimented by visual observation with fluorescence fluids under Sun illumination[4], is briefly narrated by Cardona and Merlin[5]. A detailed account of the developments with the timeline for the theoretical prediction and experimental verification of light scattering on phonons, both acoustic and optical, is provided by Fabelinskiĭ[6,7]. It is commonly accepted that the first light-scattering spectrum from thermal excitations, that is, acoustic phonons, which we now refer to as BLS or BMS, was reported in 1930 by Eugenii Gross[8–10]. He succeeded in this endeavour by developing an optical setup of several cascaded interferometers that was capable of providing the frequency dispersion needed to analyse the fine structure of spectral lines. Gross, who worked in St. Petersburg, Russia, was aware of Mandelstam's work in Moscow, and his prediction of light scattering on thermal excitations, and used his formula in the analysis of the experimental data[6,7]. However, it was not until the 1960s that experimental BLS research received new impetus with the invention of lasers and, later, the introduction of high-contrast multi-pass tandem Fabry–Pérot (FP) interferometers by John Sandercock[11].

Brillouin–Mandelstam light scattering is complementary to Raman spectroscopy, which is another inelastic light-scattering technique. In the realm of phonons—quanta of crystal lattice vibrations—a Brillouin spectrometer measures the energies of acoustic phonons, whereas a Raman spectrometer measures the energies of optical phonons. In many cases BLS spectroscopy is a more powerful technique, in the sense that, like Raman spectroscopy, it measures not only the energy of phonons near the Γ point, but it can also provide data for determining the phonon dispersion in the vicinity of the Brillouin zone (BZ) centre. Owing to the several orders of magnitude smaller energy shifts in the scattered light measured in Brillouin spectroscopy experiments than in Raman spectroscopy experiments, the BLS instrumentation utilizes FP interferometers rather than diffraction gratings. A single-plane parallel FP interferometer consists of two flat mirrors arranged parallel to each other, at the spacing of L. The wavelength of light λ, which can be transmitted through the FP interferometer, is determined by $\lambda = 2L/m$, where m is an integer. In this structure, the free spectral range of the interferometer, that is, the frequency difference between two neighbouring orders of interference, is $1/(2L)$ (cm^{-1}). The resolution of the instrument is defined by the width of the transmitted peak. The ratio of the free spectral range to the width is referred to as the finesse (F). The contrast (C)—the ratio of the maximum to the minimum transmission—is a function of the finesse as $C = 1 + 4F^2/\pi^2$, which is less than 10^4. The low contrast of the single-plane parallel FP does not allow one to distinguish the low-intensity Brillouin scattering of light from that of the elastically scattered component. The multi-pass tandem FP interferometer enhances the spectral contrast by orders of magnitude, making it possible to detect the low-intensity Brillouin scattering peaks even for opaque materials. State-of-the-art triple-pass tandem FP systems provide a contrast of 10^{15} (ref. [12]).

At present, BLS is at a similar stage of development and use similar to that of Raman light-scattering spectroscopy of around 30 years ago. The need for determining phonon and magnon dispersions in novel two-dimensional (2D) materials, nanostructures and spintronic materials has resulted in a rapid expansion of this photonic technique to new material systems. Recent developments in BLS instrumentation, like the confocal Raman spectrometer developments several decades ago, have resulted in a much wider use of inelastic BLS. This technique involves acoustic phonons and magnons, which have up to a thousand times lower energy than that of optical phonons and magnons as well as smaller scattering cross-sections. These differences explain why BLS instrumentation is more complicated than Raman spectroscopy instrumentation, and why it has taken more time develop.

Nano-Device Laboratory (NDL) and Phonon Optimized Engineered Materials (POEM) Center, Department of Electrical and Computer Engineering, University of California, Riverside, Riverside, CA, USA. ✉e-mail: fkargar@ece.ucr.edu

In the past, Brillouin spectroscopy was used mainly for determining the elastic constants of bulk materials and for examining geological samples[13]. More recently, this photonic technique has enjoyed a surge in use for investigating various physical phenomena in advanced materials and devices. It has been used to investigate the acoustic phonon spectrum changes in phononic metamaterials[14–22], and the direct observation of phonon softening in bulk materials even with a low concentration of dopants[23]. A demonstration of acoustic phonon confinement in thin-film membranes, individual semiconductor nanowires and other nanostructures has been accomplished with this technique[24–29]. Brillouin spectroscopy can measure the phonon dispersion in low-dimensional materials and small-size samples where other techniques, for example, neutron diffraction, inelastic X-ray spectroscopy, helium atom scattering and inelastic ultraviolet scattering, fail either due to the sample size or detectable energy range limitations[30]. The equipment required for these alternative techniques is expansive and voluminous. Accurate knowledge of the phonon spectrum is essential for understanding the electronic and photonic properties of materials. The application of BLS is not limited to the detection of phonons. Brillouin spectroscopy has proved to be a powerful tool for studying the quanta of spin waves (SWs), that is, magnons, which are quasiparticles that define the magnetic properties of matter. The technique has been instrumental in demonstrating the condensate of magnons[31] and has allowed the in situ monitoring of magnon propagation and interaction in spintronic devices[32–35]. The BLS technique has also been used in studying the noise of magnons in SW devices[36]. In this Review, we discuss the recent developments in physics and engineering that have been enabled using BMS and forecast the future of this innovative photonic technique. The terms BLS and BMS are used to describe spontaneous Brillouin light-scattering spectroscopy, which is different from stimulated Brillouin light scattering. In the latter, the intensity of the scattered light is enhanced by the application of a secondary laser light beam with the frequency of the excited phonons[37–39].

Fundamentals of Brillouin light scattering

It is well known that light-scattering processes depend strongly on the optical properties of materials and the penetration depth of light into the material[40]. As a result, light scattering must be treated separately for different classes of materials depending on their optical transparency at the excitation laser wavelength[11]. In certain cases, the optical selection rules imposed by the size and opacity of the material system under investigation create new opportunities for the BLS technique. In the BLS of crystal lattice vibrations, two different mechanisms contribute to the scattering of light: (1) bulk phonons via the volumetric opto-elastic mechanism and (2) surface phonons via the surface-ripple mechanism[11,41]. The dominance of one or the other in the BLS spectrum depends on the size, for example, the thickness, and the optical properties of the material, for example, the transparency or opacity of the material at the given excitation wavelength.

Scattering of light by bulk phonons. In transparent or semitransparent materials, where the penetration depth of light is sufficiently large compared with that of the incident laser light wavelength, scattering by the bulk phonons is the dominant mechanism. A propagating acoustic phonon of wavevector $\mathbf{q}$ and angular frequency ω_q induces local variations in the dielectric constant of the medium, which can scatter light through opto-elastic coupling[41,42]. A general schematic of the light-scattering process by volumetric phonons is illustrated in Fig. 1a. In all light-scattering processes, two equations, of the conservation of momentum, $\hbar\mathbf{k}_s - \hbar\mathbf{k}_i = \pm\hbar\mathbf{q}$, and the conservation of energy, $\hbar\omega_s - \hbar\omega_i = \pm\hbar\omega_q$, should be satisfied. Here $\mathbf{k}_i$ and $\mathbf{k}_s$ are the wavevectors and ω_i and ω_s are the angular frequencies of the incident and scattered light, respectively. The positive and negative signs on the right-hand side of these equations denote the 'anti-Stokes' and 'Stokes' processes, respectively. In the anti-Stokes process, a phonon is annihilated (or absorbed) whereas in the Stokes process a phonon is created (or emitted) during the scattering process. The angle between $\mathbf{k}_i$ and $\mathbf{k}_s$, ϕ, is the scattering angle, which depends on the scattering geometry[11,41]. Since the energy change in the light-scattering processes by acoustic phonons is negligible compared with that of the energy of the incident light, one can assume that $k_i \approx k_s$. Therefore, from the conservation of momentum, it is inferred that the magnitude of the phonon wavevector is $q = (4\pi n/\lambda)\sin(\phi/2)$, where n and λ are the refractive index of the material and the wavelength of the excitation laser light, respectively. In the backscattering geometry where $\phi = 180°$, the maximum detectable phonon wavevector, $q_m = 4\pi n/\lambda$, is achieved[11].

Apart from the substantial difference in the energies of the elemental excitations, the light-scattering processes in both Raman and BLS techniques are similar. The Stokes and anti-Stokes optical peaks appear as doublets on both sides of the central line in the frequency spectrum (Fig. 1b). The spectral analysis of these peaks, including the frequency shift, intensity and full-width at half-maximum, provides information about the energy, population and lifetime of the detected elemental excitations[43]. Typical Raman systems can detect the frequency range between ~3 THz (~100 cm^{-1}) and 135 THz (4,500 cm^{-1}). This is the range in which the optical phonons reside. Modern low-wavenumber Raman (LWNR) instruments utilize novel notch filters and fine gratings, which allow the detection of phonons with minimum energies of ~360 GHz (~12 cm^{-1}) or higher. The multi-pass tandem FP interferometer deployed in BLS can probe quasiparticles with much lower energies in the range of 300 MHz to 900 GHz. This spectrum interval is essential for probing acoustic phonons and magnons. Both Raman and Brillouin–Mandelstam light-scattering techniques observe phonons with wavevectors close to the BZ centre, and are limited by the wavevector of the excitation wavelength of the laser source. A combination of BLS, LWNR and conventional Raman techniques allows the detection of phonons and magnons in the frequency range from hundreds of megahertz up to tens of terahertz at wavevectors close to the BZ centre.

The dispersion of the fundamental acoustic phonon polarization branches is linear in the vicinity of the BZ centre, where the phase velocity ($v_p = \omega/k$) and the group velocity ($v_g = \partial\omega/\partial k$) are equal. In the BLS experiment, by calculating the probing phonon wavevector and measuring the peak frequency observed in the spectrum, one can determine v_p and v_g of the associated phonon mode. For example, in the backscattering geometry, which is widely used, $v_p = \lambda f/(2n)$ in which f is the spectral position of the associated peak observed in the BLS spectrum. Since optical phonons have a flat dispersion in the vicinity of the BZ centre, determining q is not essential in most Raman experiments. Figure 1c shows the dispersion of the longitudinal (LA) and transverse (TA) acoustic phonons and the longitudinal (LO) and transverse (TO) optical phonons in silicon along the [001] direction. Figure 1d provides the actual accumulated Raman and BLS spectra of silicon.

Scattering of light by surface phonons. In opaque and semitransparent materials, the BLS spectrum is dominated by the scattering of light by surface phonons via the ripple mechanism[11,41]. The process is illustrated schematically in Fig. 1e,f. Owing to high optical extinction in these types of materials, the penetration depth of light is limited to the surface, and only the in-plane component (parallel to the surface in the scattering plane) of the phonon momentum-conservation law is satisfied. Therefore, only phonons with the in-plane wavevector component, $q_{\parallel} = k_i \sin(\theta_i) - k_s \sin(\theta_s)$, where θ_i and θ_s are the incident and scattered light angle, respectively, with respect to the normal to the surface, may contribute to the light scattering (Fig. 1f). In a complete backscattering geometry

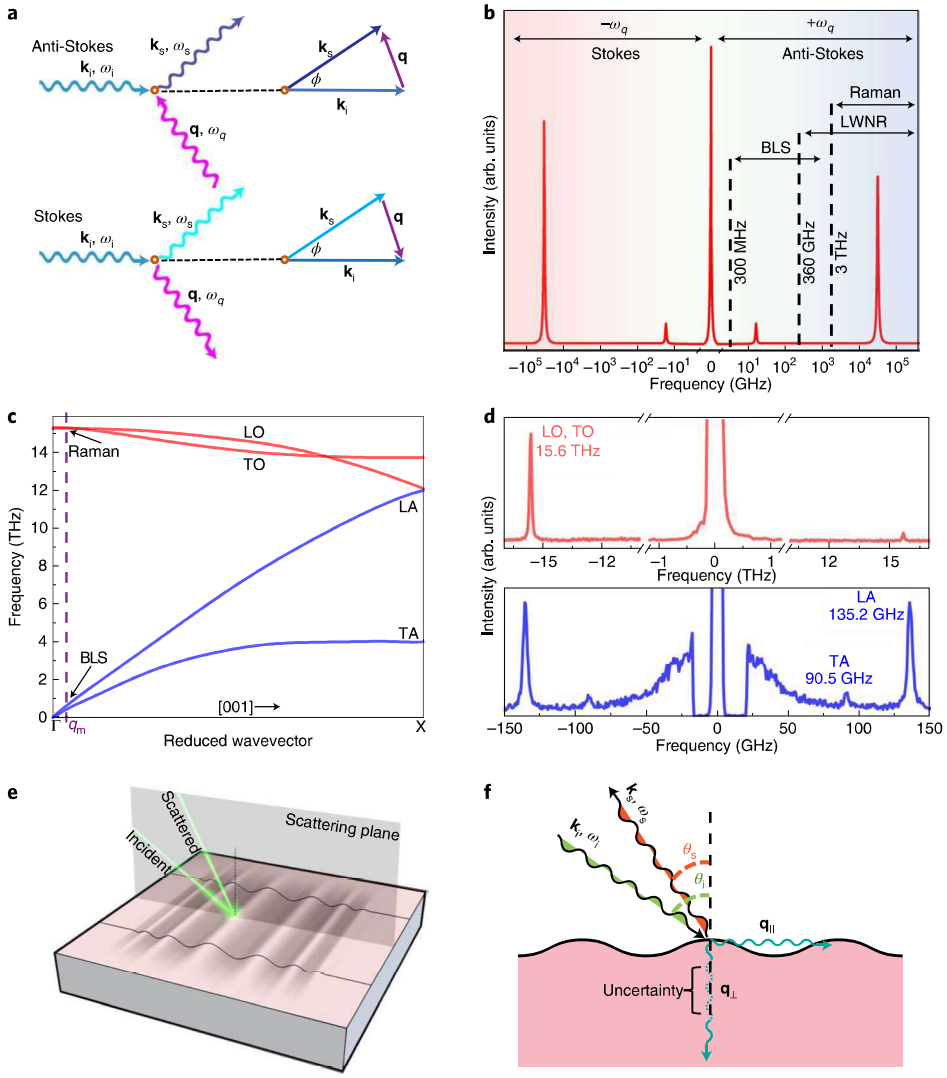

Fig. 1 | Fundamentals of Brillouin–Mandelstam light scattering. a, Schematic of the light-scattering processes via bulk quasiparticles. The incident light with wavevector, $\mathbf{k}_i$, and frequency, ω_i, is scattered to the $\mathbf{k}_s$, ω_s state either by absorbing (anti-Stokes process) or emitting (Stokes process) a quasiparticle with the wavevector and energy of $\mathbf{q}$, ω_q, satisfying the momentum- and energy-conservation laws. The scattering angle, ϕ, is defined as the angle between $\mathbf{k}_i$ and $\mathbf{k}_s$. **b**, Schematic showing the typical spectra and accessible phonon frequency ranges using the Raman, LWNR and BLS techniques. **c**, Phonon dispersion in silicon crystal along the [001] direction. The dashed line indicates roughly the maximum wavevector of both optical and acoustic phonons that can be detected by optical techniques. **d**, Raman (upper) and BLS (lower) spectra of silicon showing the TO and LO phonons at 15.6 THz and the TA and LA phonons at 90.5 GHz and 135.2 GHz at $q = 9.8 \times 10^5$ cm^{-1}, respectively. **e**, Schematic showing light scattering by the surface-ripple mechanism in semitransparent, opaque and thin-film materials. **f**, Side view of the ripple scattering process where θ_i and θ_s are the incident and scattered angles of light with respect to the normal to the surface, and $\mathbf{q}_\parallel$ and $\mathbf{q}_\perp$ are the in-plane and normal wavevector components of the phonons participating in the scattering.

where $\theta_i = \theta_s = \theta$, the in-plane phonon momentum is $q_\parallel = (4\pi/\lambda)\sin(\theta)$. Note that, here, the phonon wavevector depends only on the incident angle and excitation laser wavelength. Under such conditions, one can probe phonons with different wavevectors by changing the incident angle of the laser light. The latter allows one to obtain the phonon dispersion that is the energy (frequency) of the phonons as a function of the wavevector. In the backscattering BLS configuration, considering a semi-infinite elastically isotropic material (Fig. 1e,f), the scattering cross-section is given as $d^2\sigma/d\Omega\, d\omega_s = \left(\zeta\omega_i^4/16\pi^2c^4\right)\xi^2\,|u^z(0)|^2_{q_\parallel,\omega}$ in which ζ and c are the sample area under illumination and the speed of light in a vacuum, respectively. The parameter ξ is a coefficient which depends on θ_i, θ_s and the relative permittivity of the scattering medium. The last term, $|u^z(0)|^2_{q_\parallel,\omega}$, is the mean square displacement of the surface perpendicular to $q_\parallel$ in the scattering plane[44]. In fact, it is the last term that determines which phonon modes contribute to the light scattering. As it is seen, only those surface phonons with a vibrational displacement perpendicular to $q_\parallel$ in the plane of scattering appear in the BLS spectrum. Obtaining the energy dispersion of the elemental excitations is a distinctive advantage of the BLS technique over Raman spectroscopy. Modifications in the phonon dispersion and, correspondingly, in the phonon density of states contain a wealth of information on confinement and proximity effects in low-dimensional material systems[45,46].

Phonons in nanostructured materials

Phonons reveal themselves in the thermal, optical and electronic properties of materials[46,47]. Similar to electron waves, the phonon spectrum in nanostructures undergoes changes as a result of either decreasing the physical boundaries to nanoscale dimensions in individual structures[45] or as a result of imposing artificial periodicity[14,15,48]. The latter type of structures, where the phonon

dispersion is intentionally modified, are referred to as phononic crystals (PnCs)[49]. The terminology is similar to photonic crystals (PtCs) where the propagation of light in the crystal structure is modified by creating an artificial periodic pattern with a characteristic period. Using the same concept of periodic patterning a new type of structure, termed the phoxonic crystal (PxC), has also been introduced that modulates both the phonon and photon dispersions concurrently[14,50]. In PxCs, the simultaneous modulation of the elastic and electromagnetic properties is achieved by tuning the material properties such as the dielectric constant and mass density, the periodic pattern, as well as the shape of the individual elements[14,50]. Direct observation of phonon-state modifications in the hypersonic frequency range, both in the confined regime or in periodic nanostructured materials, is challenging due to the required high spectral and spatial lateral resolutions. Recent reports have demonstrated that BLS spectroscopy is an effective technique for observing acoustic phonons in these nanostructured material systems, which typically have lateral dimensions in the range of a few micrometres[14–21].

Phonon confinement in individual nanostructures. In the phonon-confinement regime, additional phonon polarization branches appear with optical phonon-like properties such as non-zero energy ($\omega(q=0)\neq 0$) at the Γ point and a nearly flat dispersion at the BZ centre. These modes are substantially different from the fundamental LA and TA modes, which have zero energies at the Γ point. Confined acoustic (CA) phonons in different structures share common characteristics, such as (1) a non-zero energy at the BZ centre ($\omega(q=0)\neq 0$); (2) quasioptical dispersion in the vicinity of the BZ centre characterized by a large v_p but a near-zero v_g; (3) a decrease in energy difference between different phonon branches with increasing structure dimensions, for example, the nanowire diameter; and (4) hybrid vibrational displacement profiles, that is, consisting of vibrations along different crystallographic directions[45]. Recent studies have reported the direct observation of phonon confinement effects in individual nanostructures such as nanowires[24,51], thin films[26,27], nanospheres[25], nanocubes[28] and core–shell structures[52,53] using BLS. In such structures with nanometre-scale dimensions, light scattering by the surface-ripple mechanism dominates the spectrum. Figure 2a presents the measured phonon spectrum of a set of long GaAs nanowires with a diameter, D, of 122 nm and a large inter-nanowire distance (red curve) together with the reference GaAs substrate without the nanowires (blue curve)[24]. The inset shows the scanning electron microscopy (SEM) image of the representative sample. The large inter-nanowire distance ensures that modification of the phonon spectrum is achieved in the individual nanowires. One can see that the fundamental TA and LA phonon peaks are present in both spectra. The additional peaks are the CA phonons in individual nanowires. In the spectrum, the CA phonons are lower in frequency than the bulk TA and LA peaks because the probing phonon wavevector is different. Figure 2b shows the spectral position of the peaks (symbols) determined using Lorentzian fitting[24]. The data are plotted over the theoretical phonon dispersion calculated from the elasticity equation for an individual nanowire with the diameter obtained from SEM image analysis. The normalized displacement ($\bar{u}$) profiles for a nanowire at $q=18.0\,\mu m^{-1}$ and at different frequencies confirm the hybrid nature of these vibrational modes (Fig. 2c). The vibrational profile of different phonon modes determines the phonon modes that are likely to appear in the BLS spectrum. These results demonstrate the power of BLS for obtaining the energy dispersion $E(q)$ or $\omega(q)$ data for individual nanostructures in the samples of small size.

Two decades ago, it was suggested theoretically that the spatial confinement of acoustic phonons can modify their phase and group velocity, phonon density of states and the way that acoustic phonons interact with other phonons, defects and electrons[54,55]. However, direct experimental evidence of such effects was missing. The debated question was also the length scale at which the velocity of phonons undergoes significant changes. A detailed BLS study on silicon membranes with various thicknesses (d) in the range of 7.8–400 nm confirmed that the phase velocity, v_p, of the fundamental flexural mode experiences a dramatic drop of 15-fold for membranes with $d\leq 32$ nm (ref. [26]). Figure 2d shows the effect of the membrane thickness on the phonon dispersion as a function of the dimensionless wavevector $q_{\|}d$ (ref. [26]). Note the data enclosed in the dashed box for ultrathin membranes, where the phase velocity is significantly lower than the fundamental TA and LA modes as well as the pseudo-surface-acoustic-wave in bulk silicon in the [110] direction. Similar to nanowires and thin membranes, multiple CA phonon modes have been observed in closely packed silica (SiO_2) nanospheres of 200–340 nm diameter[25]. The acoustic modes are quantized due to the spatial confinement causing the BLS spectrum to be overloaded with many well-defined Lorentzian-shaped peaks. The spectral position of these peaks is inversely proportional to the diameter of the nanosphere (Fig. 2e). The solid lines in Fig. 2e show the theoretical Lamb spheroidal frequencies of the nanospheres, ν_{nl}, where $l=0,1,2,...$ is the angular momentum quantum number and n is the sequence of eigenmodes in increasing order of energy. The BLS selection rules only allow the modes with even numbers of l to appear in the spectrum[56]. It should be noted that these peaks do not originate because of the periodicity of nanospheres as their spectral position does not vary with changing the direction of the phonon probing wavevector in the BLS experiment. The direction of the probing wavevector can be changed simply by the in-plane orientation of the sample during BLS experiments. The spectral position of the observed peaks plotted as a function of the inverse diameter confirms that the energy of the vibrational eigenmodes decreases with increasing diameter. Other studies have reported similar confinement effects in GeO_2 nanocubes[28]. So far, no BLS experiments have been reported to demonstrate acoustic phonon confinement in quantum dots with diameters in the range of a few nanometres.

The phonon spectrum and related material properties, such as the thermal conductivity or electron mobility, can be tuned by embedding nanostructures in the materials with a large acoustic-impedance mismatch[45]. The acoustic impedance is defined as $\zeta=\rho v_s$, where ρ and v_s are the mass density and sound velocity, respectively, of each constituent. In this case, the phonon dispersion of the embedded material depends not only on the diameter, the properties of the material and the surface boundary conditions but also on the properties of the embedding material, for example, a barrier layer or coating[45]. Interfacing layers of materials with nanometre-scale thicknesses or diameters with a large acoustic-impedance mismatch is part of the phonon-engineering approach. One can also consider it the phonon proximity effect, borrowing the terminology from the spintronic and topological insulator fields. Figure 2f presents the BLS data for a core–shell structure, where the rigid core silica nanospheres with a diameter of 181 ± 3 nm are coated by softer thin layers of poly(methyl methacrylate) shells with average thicknesses of 25, 57 and 112 nm (ref. [52]). The resulting samples are core–shell particles with the outer diameter d ranging from 232 to 405 nm. For bare silica, two phonon peaks are observed at 13 and 19 GHz. For the core–shell samples, the frequency of these two peaks is suppressed due to the proximity effect of the softer coating layer on the rigid core. As the thickness of the shell increases, the number of vibrational resonance modes in the investigated frequency range also grows (Fig. 2f, bottom). The vibrational profiles of these structures for various values of l are shown in Fig. 2g.

Phonons in periodic structures. As defined previously, PnCs are a class of materials that consist of an array of holes or pillars arranged in specific lattice configurations[49]. Figure 3a shows schematics of square-lattice solid-hole (top) and solid-pillar (middle) PnC structures. The periodic modulation of the elastic constants and the mass

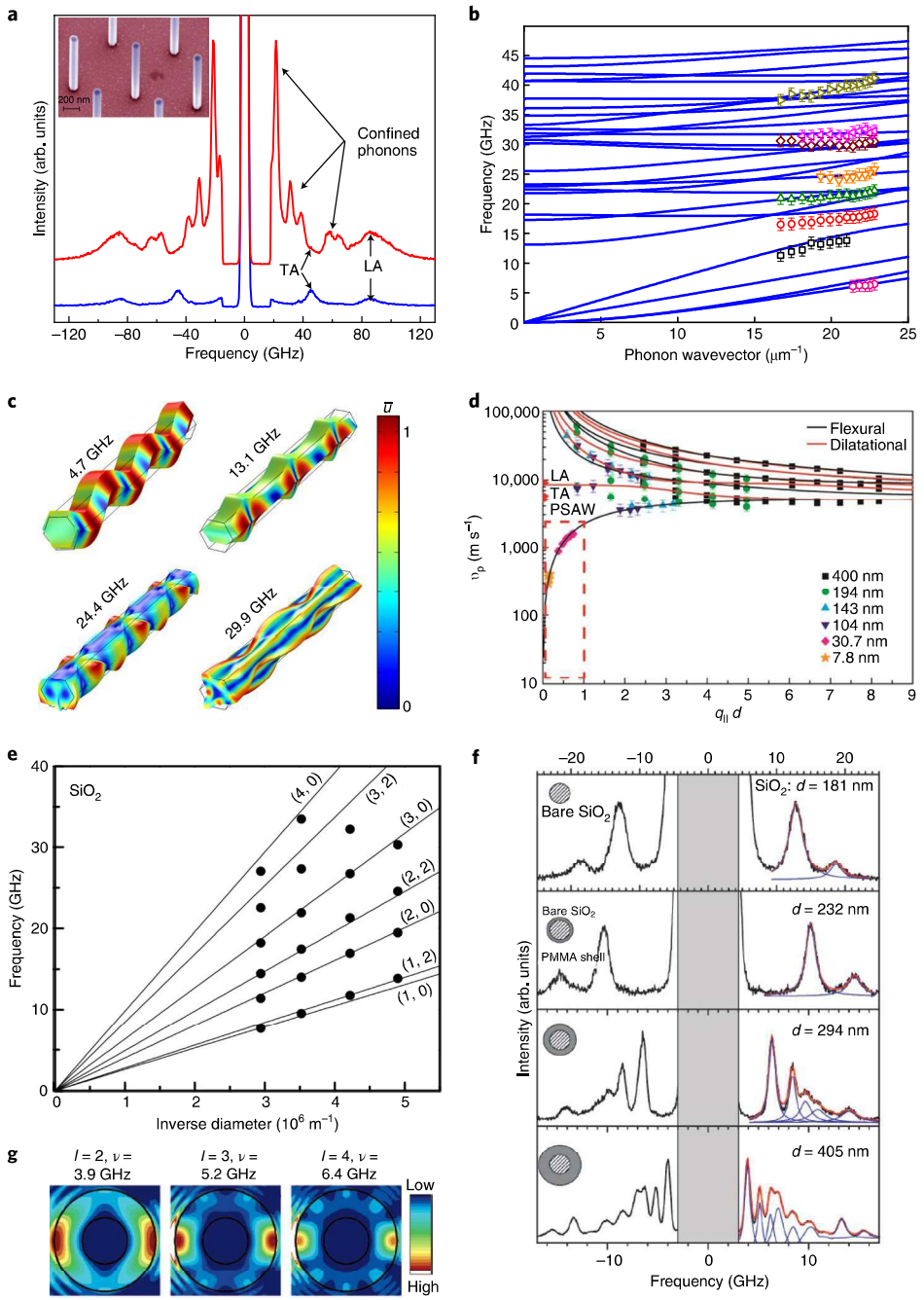

Fig. 2 | Observation of phonon confinement in nanostructured materials via the BLS technique. a, Measured BLS spectra of GaAs nanowires with $D = 122$ nm (red curve) grown on a GaAs substrate, and of a pristine substrate (blue curve). The fundamental TA and LA phonons are present in both spectra. Extra peaks in the red curve correspond to the CA phonons. The inset shows a pseudo-colour SEM image of the nanowires. **b**, Measured (symbols) and calculated (blue curves) phonon dispersion of the same GaAs nanowires. **c**, Normalized displacement ($\bar{u}$) profiles of confined phonons contributing to BLS. **d**, Phase velocity of confined phonon modes determined from measured BLS data as a function of the dimensionless wavevector for silicon membranes. The velocity values of the fundamental TA and LA modes and the pseudo-surface-acoustic-wave (PSAW) in the [110] direction of bulk silicon are shown with red symbols for reference. **e**, Spectral position of confined phonon peaks (black dots) of silica nanospheres plotted on theoretical frequencies of vibrational eigenmodes denoted by (n, l) as a function of the inverse diameter. The numbers n and l denote the sequence of eigenmodes and the angular momentum quantum number, respectively. **f**, BLS spectra of a silica nanosphere (top) and core–shell silica nanospheres coated with poly(methyl methacrylate) (PMMA). Note the difference in the frequency scales of the top and bottom axes. The blue and red curves are the individual and cumulative fitting to the actual BLS data, respectively. **g**, Displacement profiles of the first three resonance modes of the 405 nm core–shell particle. ν is the frequency. Panels adapted with permission from: **a**,**c**, ref. [24], Springer Nature Ltd. Panels reproduced with permission from: **b**, ref. [24], Springer Nature Ltd; **d**, ref. [26], American Chemical Society; **e**, ref. [25], APS; **f**,**g**, ref. [52], American Chemical Society.

density defines the phonon propagation properties. The dimensions of the holes and the period of the artificial lattice define the range of frequencies in which the phonon properties can be engineered[49]. Typically, to modify phonons in the hypersonic frequency range, one needs to fabricate structures with a characteristic size of a few tens to hundreds of nanometres[48]. Additional phonon branches appear

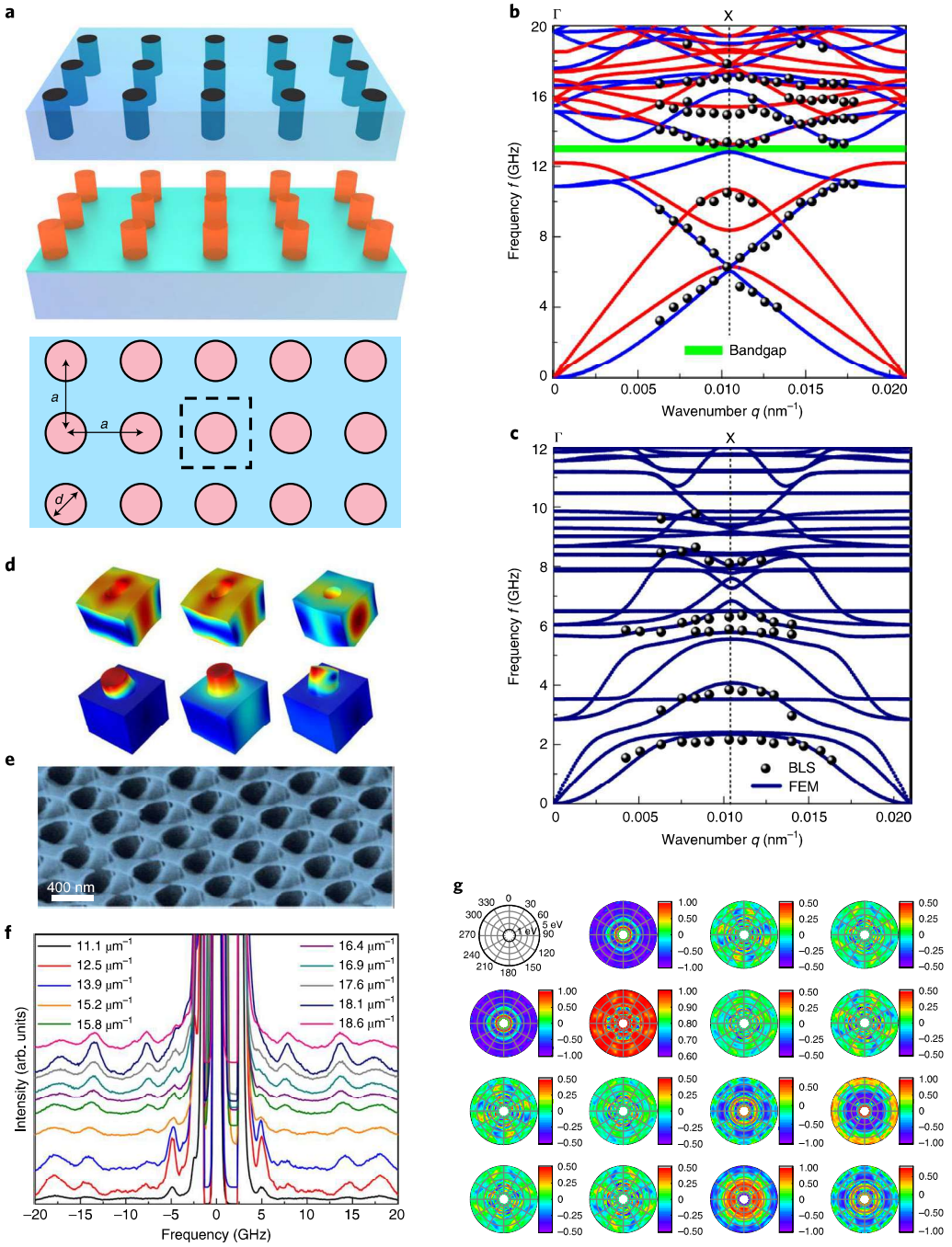

Fig. 3 | Phonon spectrum modification in PnCs and PxCs investigated using the BLS technique. a, Schematics showing the top and side views of holey- and pillar-based PnCs, representing two approaches for engineering the phonon dispersion via artificial periodicity. *a*, lattice constant; *d*, diameter. **b**, Measured (black dots) and calculated phonon dispersion of a holey silicon PnC with a square lattice ($d = 100$ nm and $a = 300$ nm) along the Γ–X direction. Note the appearance of the phononic bandgap depicted by the green band. **c**, Measured (black dots) and calculated phonon dispersion in a gold pillar-based PnC along the Γ–X direction. **d**, Examples of displacement profiles of holey- (upper) and pillar-based (lower) PnCs. **e**, Side-view SEM image of a silicon pillar-based PxC with designed pillar shapes, revealing the simultaneous modification of the phononic and photonic properties. **f**, BLS data of the structure shown in **e** at different probing phonon wavevectors. The spectral position of the BLS peaks is not altered by changing the phonon wavevector, confirming the flat dispersion of the phonon branches. **g**, Polar contour plots of the normalized indices of Mueller matrix spectroscopic ellipsometry data at an incident angle of 70°, showing four-fold symmetry for the optical modes in the same structure. Panels reproduced with permission from: **b**,**c**, ref. [16], APS; **e**–**g**, ref. [14], IOP. Panel **d** adapted with permission from ref. [16], APS.

in the spectrum of a PnC due to localization of phonon modes in its individual constituents or as a result of Bragg scattering in the periodic structures[15]. The dispersion and energy of these phonon modes can be tailored via changing the characteristic dimensions and the lattice arrangement of the holes or the pillars.

Recent years have witnessed an explosive growth of the use of the BLS technique for the investigation of acoustic phonon modulation in 1D, 2D and 3D PnCs[14–22]. Figure 3b shows the measured (black spheres) and calculated (solid lines) phonon polarization branches along the Γ–X direction in a holey square-lattice PnC

fabricated through patterning a 250-nm-thick suspended silicon membrane[16]. The hole diameter and the lattice constant in this structure are $d = 100$ nm and $a = 300$ nm, respectively. Note that the artificial periodicity causes the BZ edge to shrink to $\pi/a \approx 10.47\ \mu m^{-1}$, which is almost three orders of magnitude smaller compared with that of bulk silicon. In this structure, one expects to observe many phonon modes as a result of both phonon confinement in the silicon membrane and phonon folding from the reduced BZ edges owing to the imposed periodicity. Two BLS experiments, one on the pristine silicon membrane and another on a silicon membrane with air holes, allow one to assign the associated BLS peaks to either confined phonons or folded phonons. Phonon folding results in the opening of a small energy bandgap in the Γ–X direction. In this bandgap region, illustrated by the green rectangular band in Fig. 3b, the propagation of any acoustic waves is prohibited. Pillar-based PnCs allow one to tailor the phonon dispersion by arranging short pillars on top of the bulk substrate or thin membranes[49]. Figure 3c shows the measured and calculated phonon dispersion of a silicon membrane with gold cone-like pillar structures in the square-lattice configuration[16]. The flat dispersion of phonon polarization branches is probably the result of phonon localization in the pillar structures. The vibrational displacement profile of the phonon branches is calculated using the elasticity continuum equation. The results of numerical simulations of the vibrational modes of a few phonon branches in the air–solid and pillar-based PnCs are presented in Fig. 3d[16]. The red colour represents larger displacements. Note the localized modes in the individual pillars for the pillar-based PnCs. The data obtained using BLS are essential for the experimental validation of models used for the calculation of phonon dispersions and displacements.

In PxCs, the phonon and photon states are tailored in the same periodic structure[50]. Simultaneous tuning of the properties of visible light and acoustic phonons in a specific energy interval requires structures with a periodicity in the range of a few hundred nanometres. A proper design of the lattice geometry and dimensions with contrasting elastic and dielectric properties in PxCs creates an exciting prospect for engineering and enhancing the light–matter interaction[57]. Such structures can be utilized in designing novel optoelectronic devices such as phoxonic sensors[58] and optomechanical cavities[59]. Figure 3e shows an SEM image of a designer silicon-on-silicon 'pillars with the hat' PxC in the square-lattice configuration[14]. The BLS spectra and the normalized Mueller matrix indices (m_{ij}, $i,j = 1,...,4$) of spectroscopic ellipsometry data for phonons and photons are shown in Fig. 3f,g, respectively. The spectral position of the BLS peaks shown in Fig. 3f does not vary with changing the phonon wavevector, confirming that the flat dispersion of the phonon polarization branches is a result of artificial periodicity. BLS measurements along different quasicrystallographic directions of the PxC allow for disentangling the phonon confinement in individual elements of the structure from phonon folding due to the periodicity. Figure 3g exhibits each element of the Mueller matrix normalized by m_{11}. The Mueller matrix describes the light interaction with an optical element including depolarization and scattering effects by relating the incoming Stokes vector ($\mathbf{S}_i$) to the outgoing Stokes vector ($\mathbf{S}_o$). The ellipsometry data indicate that the light-propagation characteristics are also affected by the structure periodicity. The PxC structure is substantially different from that of conventional PtCs where, typically, silicon pillars are fabricated on a low-refractive-index layer, for example, silica, to minimize the optical losses[60].

Detection of spin waves using Brillouin light scattering

In recent years, BLS has become a standard technique for the visualization of SWs and their interactions with other elemental excitations in magnetic materials[61–64]. Magnons contribute to light scattering through magneto-optic interactions. The details on how magnons scatter light have been explained in ref. [65]. The scattering of light by bulk magnons follows the same rules of conservation of momentum and energy as described earlier. In the case of surface magnons, such as propagating Damon–Eschbach modes, the in-plane component of the light-scattering process is sufficient to define the magnon's wavevector[11].

BLS has several advantages over other experimental techniques, such as ferromagnetic resonance (or FMR), microwave absorption or inelastic neutron scattering, used for detecting SWs[61]. These advantages can be summarized: (1) high sensitivity for detecting weak signals from thermally excited incoherent magnons, even in ultrathin magnetic materials; (2) high space and wavevector resolution for mapping of SWs; (3) the simultaneous detection of SWs with different frequencies; (4) a wide accessible frequency range, which became possible with FP interferometry; and (5) its compactness of instrumentation[61]. In addition, recent developments in phase- and time-resolved BLS have provided an efficient platform for studying the propagation of externally excited coherent SWs[66]. A temporal resolution of 1–2 ns can be achieved in conventional BLS systems by adding the time-of-flight single-photon counting methodology[67]. The phase information for SWs can be obtained by studying the interference patterns of inelastically scattered light from the SW under investigation and the coherent reference signal. Details of the phase-resolved BLS system can be found in ref. [68]. The BLS technique can provide information about the spatial, phase and temporal evolution of SWs in magnetic systems. The combination of all these features has made BLS an essential tool for recent advancements in magnonic research, which include the submicrometre spatial mapping of externally excited SWs[69–72], observation of the Bose–Einstein condensation (BEC) of magnons[31,73] and investigation of the Dzyaloshinskii–Moriya interaction (DMI)[74–77]. In all these examples of the use of BLS, it is important for the excitation laser beam to be positioned precisely on the magnetic samples, with micrometre-scale lateral dimensions and keep it stable over the long data-accumulation times[61]. With modern-day instrumentation, these requirements are satisfied in fully automated micro-BLS (μ-BLS), which can monitor and compensate for the positional displacement of the sample due to temperature drifts[61]. Below, we describe the recent breakthroughs achieved in the spintronic–magnonic field using BLS and μ-BLS systems in more detail.

Magnon currents or SWs can be externally excited in magnetic waveguides using antennas and microwave currents. A number of studies have been devoted to investigating SW transport in waveguides implemented with ferrimagnetic insulators, for example, yttrium iron garnet (YIG), ferromagnetic materials such as permalloy (Py) or other material systems[32,70–72,78,79]. By spatially mapping the intensity of the magnon peak in the Brillouin spectrum as a function of the distance from the emitting antenna, one can determine the SW decay length or damping parameter[69–72,78,80,81]. The high sensitivity of BLS allows the detection of magnon peaks even at millimetre-scale distances from the emitting antenna[35]. BLS detects non-linear effects such as second-order SWs in multi-magnon scattering processes[79,80]. Figure 4a shows an optical microscopy image of a 2D Y-shaped SW multiplexer in which the SW dispersion and propagation in Py can be controlled by the local magnetic fields induced by the current applied to each gold conduit[72]. The SWs are launched into the structure by a microwave antenna in the frequency range between 2 and 4 GHz, and are routed to either the left or right arm by passing the d.c. current ($I_{d.c.}$) to connect, respectively, either switch S1 or S2. The BLS peak intensity as a function of the excitation frequency in each arm at 4.5 μm distance from the Y junction is presented in Fig. 4b. The spectra confirm the possibility of efficient SW switching in this waveguide design. Figure 4c presents a 2D BLS intensity map of SW propagation at 2.75 GHz excitation, which clarifies that the SW travels in the same direction as the current flow.

The magnon Bose–Einstein condensate at room temperature in magnetic materials is one of the most intriguing findings

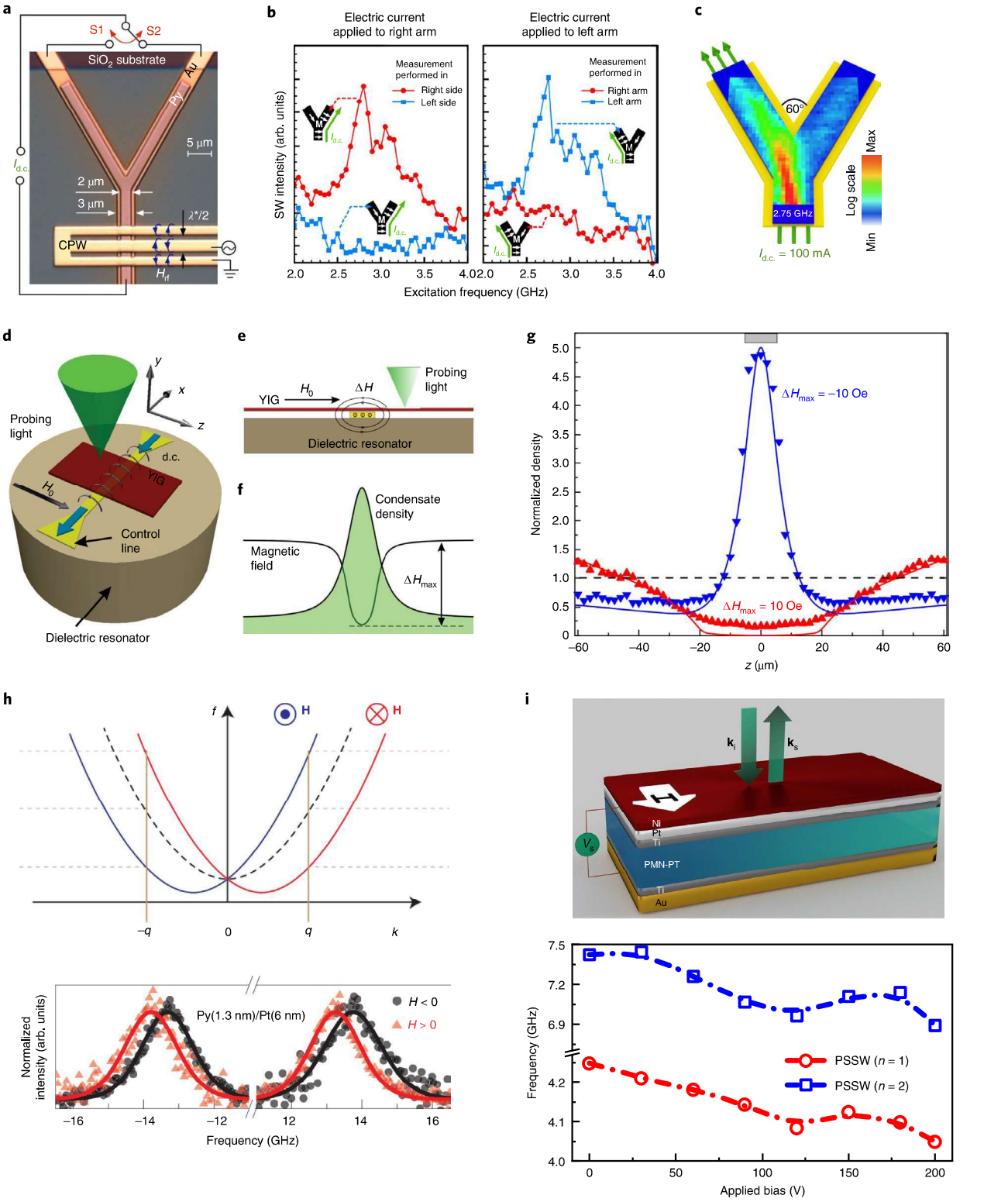

Fig. 4 | Investigation of spin waves using BLS. a, SW propagation in a Y-shaped waveguide. CPW, coplanar waveguide; λ^*, wavelength of the excited SW; H_{rf}, oscillting magnetic field. **b**,**c**, Measured BLS intensity of propagating SWs inside the left and right arms. **M**, magnetization. **d**,**e**, Schematic and side view of the BEC experiment with magnons excited in the YIG by the dielectric resonator. H_0, external field; ΔH, locally created non-uniform magnetic field. **f**, Spatial distribution of magnetic field, $H_0 + \Delta H$, and magnon condensate density. **g**, The normalized condensate density in the potential well (blue) and hill (red). **h**, Top: SW dispersion with (solid) and without (dashed) the interfacial DMI. Bottom: DMI-induced asymmetry in BLS Stokes and anti-Stokes SW peak frequencies. **i**, Frequency change of the first two PSSW modes ($n = 1,2$) in nickel film on PMN-PT piezoelectric substrate as a function of bias and correspondingly, biaxial strain. Panels reproduced with permission from: **a**–**c**, ref. [72], Springer Nature Ltd; **d**–**f**, ref. [73], Springer Nature Ltd; **h**, ref. [74], Springer Nature Ltd; **i**, ref. [90], Elsevier. Panel **g** adapted with permission from ref. [73], Springer Nature Ltd.

demonstrated with this technique[31]. It has been postulated that BEC is achieved if the magnon density exceeds a critical value either by decreasing the temperature or by increasing the external excitation of the magnons[31,82]. Previously, BEC was demonstrated at low temperatures[83]. BEC can occur at relatively high temperatures if the flow rate of the energy pumped into the system surpasses a critical power[31]. In the first BEC demonstration with Brillouin scattering[31], magnons were excited in a YIG film by an external microwave parametric pumping field with a frequency of $2\nu_p$, such that $\nu_p > \nu_m$ in which ν_m is the minimum allowable frequency of the magnon dispersion at the uniform static magnetic field[31]. The pulse width of the pumping ranged from 1 to 100 µs. The microwave photon with a frequency of $2\nu_p$ creates two primary excited magnons with a frequency of ν_p with the opposite wavevectors. The intensity and frequency of the magnon peaks were recorded using time-resolved BLS at the delay times after pumping in the range of hundreds of nanoseconds. The scattering intensity, I_ν, at a specific frequency is proportional to the reduced spectral density of the magnons, which is proportional to the occupation function of the magnons, n_ν. The utilization of an objective with a large numerical aperture (or NA) allowed the capture of magnon modes with a wide range of wavevectors. The growing intensity, the decreasing frequency of the magnon modes from ν_p to ν_m for larger delay times, and the spontaneous narrowing of the population function[31,84] indicated that the excited magnons were condensed to the minimum valley of the magnon band at room temperature.

These experimental results led to intensive developments in the field. One theoretical study argued that in the implemented scheme the magnon condensate would collapse owing to attractive inter-magnon interactions[85]. However, other experimental and theoretical studies demonstrated that the interaction between magnons in the condensate state is repulsive, leading to the stability of the magnon condensate[73,82]. The schematic and cross-section of the experiment is shown in Fig. 4d,e[73]. The dielectric resonator at the bottom parametrically excites the primary magnons in the YIG film similar to the previous study[31]. The d.c. current in the control line, placed between the resonator and the YIG film, creates a local non-uniform magnetic field, ΔH, which adds to the static uniform magnetic field H_0. The spatial distribution of the condensate magnons is probed by µ-BLS along the magnetic field by focusing the laser beam on the YIG film surface. The local variation of the magnetic field creates either a potential well or a potential hill depending on its orientation, which adds to the uniform static magnetic field (Fig. 4f). Figure 4g shows the recorded BLS intensity representing the condensate density along the 'z' direction[73]. These results are obtained under the stationary-regime experiments where both the pumping and the inhomogeneous field are applied continuously. They show that in the case of a potential well, $\Delta H_{max} = -10$ Oe, the maximum condensate density occurs in the middle of the control line and it reduces significantly outside the potential well. In the case of a potential hill, $\Delta H_{max} = +10$ Oe, the opposite behaviour is observed where the density of the condensed magnons shrinks at the centre, and it gradually increases towards the outside of the hill. The latter suggests that the condensed magnons tend to leave the area of the increased field resulting in a minimum condensed density at the centre. This behaviour contradicts the assumption of the attractive inter-magnon interaction and necessitates a repulsive interaction among the condensed magnons[73].

It is known that BLS is one of the very few techniques that can be used to investigate the DMI strength in magnetic materials and heterostructures[74–77]. The DMI is a short-range antisymmetric exchange interaction in material systems lacking space inversion symmetry. It leads to the non-reciprocal propagation of SWs, thus providing a way to quantify its strength. The Brillouin spectrum consists of the frequency-wise symmetric phonon and magnon peaks associated with Stokes and anti-Stokes processes (Fig. 1b). Owing to the asymmetry induced by the DMI in the dispersion of the SWs, a small detectable frequency difference occurs between the Stokes and anti-Stokes peaks with the wavevectors of $-q$ and q, respectively. Without the DMI, the SW dispersion is frequency-wise symmetric and there would be no energy difference between SWs with q and $-q$ wavevectors. This is shown schematically in the upper panel of Fig. 4h. The dashed and solid curves show the dispersion of the SWs in the absence of the DMI and with the DMI for $q_{\parallel} \pm x$ and an in-plane magnetization of $M_{\parallel} \pm z$, respectively[74]. The high sensitivity of the BLS technique allows detection of the even a small frequency difference caused by a weak DMI interaction. The lower image of Fig. 4h shows the actual BLS data for a heterostructure of a 1.3-nm-thick Py ferromagnetic layer on a 6-nm-thick high-spin–orbit heavy metal platinum layer at a fixed $q = 16.7\ \mu m^{-1}$ under an external magnetic field of ±295 mT (ref. [74]). Note the frequency difference of the spectral positions of the Stokes and anti-Stokes peaks, which is ~0.25 GHz.

Magnon spatial confinement effects and magnonic crystals. Similar to phonons, magnon dispersion can be modified due to the size effects in individual structures[67,86–91] or in the periodic magnetic structures referred to as magnonic crystals[61,92]. Several studies have reported modifications in the magnon energy dispersion in such structures using the BLS technique[61,67,86–92]. The dispersion of magnons can also be tuned by external stimuli induced via strain[90]. Figure 4i (top) shows a structure in which a thin polycrystalline layer of nickel, a magnetostrictive material, is deposited on a PMN-PT ($[Pb(Mg_{1/3}Nb_{2/3})O_3]_{(1-x)}$–$[PbTiO_3]_x$) piezoelectric substrate[90]. The finite thickness of the nickel layer results in quantization of the magnon states, giving rise to perpendicular standing spin waves (PSSWs) across the nickel layer. By applying a d.c. voltage (V_s) to the piezoelectric substrate, a strain field is induced and the energy of the PSSW modes downshifts owing to the magneto-elastic coupling effect (Fig. 4i, bottom). In this BLS study, the non-monotonic dependence of the PSSW modes is attributed to the difference in the pinning parameters at the nickel–air and nickel–substrate interfaces.

Outlook

In recent years, BLS has proved itself as a versatile non-destructive photonic technique for applications in solid-state physics and engineering research. The capabilities offered by BLS have already resulted in advancements in the fields of low-dimensional magnetic[61,62,67,92] and non-magnetic materials and nanostructures[5,6,15,18], polymers[93–98], biological systems[99–101] and imaging microscopy[102–105]. One can foresee that this technique will find even broader use in investigations where the handling of small-size samples and detecting elemental excitations with small energies are essential. The prospective future research directions for BLS include, but are not limited to, the observation of topological and protected phonon states in phononic metamaterials[106–109], phonon chirality[110,111], the observation of phonons in the hydrodynamic regime[112–114] and investigation of the interaction of elemental excitations in bulk and low-dimensional magnetic and ferroelectric materials[33,43,115,116]. BLS is promising for studying the theoretically predicted topologically protected phonon states and one-way acoustic-wave-propagating modes in phononic metamaterials[106–109]. BLS can provide the full dispersion of hypersonic phonon modes, in the gigahertz frequency range, through the complete first- and higher-order BZs[14,15]. The artificial periodicity of phononic metamaterials shrinks the BZ to an accessible range of wavevectors that are detectable using BLS. It is expected that once the obstacles regarding the fabrication of such complicated material systems with topologically dependent properties have been addressed, BLS will become the preferred experimental approach since other non-optical methods would fail due to either sample-size limitations or the complicated nanofabrication required for carrying out other types of measurement.

One can envision a broader use of BLS in the study of phonons in graphene and other quasi-2D and quasi-1D van der Waals materials. Despite more than a decade of investigation into phonon thermal transport in graphene, there remain many open questions. For example, the Grüneisen parameter, and even the velocities of acoustic phonon modes, which carry heat in graphene, have not been accurately measured yet. The problem is that conventional BLS spectrometers have been limited by their inability to locate samples with lateral dimensions smaller than a few micrometres as the samples are rotated, in addition to the reduced light-scattering cross-section in low-dimensional materials. Moreover, the detection of elemental excitations with frequencies lower than around 1 GHz is challenging. At the phonon wavevectors of interest, the out-of-plane TA phonon frequencies in graphene and many other 2D materials are lower than the cut-off frequency. The state-of-the-art BLS systems are capable of measuring frequencies down to ~300 MHz, which is important for the observation of out-of-plane (ZA) acoustic phonons in graphene and other low-dimensional materials. Technically, the minimum accessible frequency is limited by the excitation laser's linewidth, which is ~100 MHz for BLS applications. The small scattering cross-section for many light-scattering processes in low-dimensional materials requires long data-accumulation times. Modern BLS systems equipped with additional anti-vibrational systems can overcome this hurdle and can be run for days of measurements. Phonon chirality is another interesting concept in low-dimensional materials, which has been experimentally demonstrated via indirect measurements[110,111]. It is anticipated that BLS can provide a direct observation in certain material systems with tailored dimensions and structures. Another use for the BLS technique can be derived from a classical theoretical study, which suggests that Brillouin spectroscopy would be a suitable technique for investigating phonons in the hydrodynamic regime, where macroscopic collective phonon transport occurs[112]. In this region, phonon transport is neither ballistic nor diffusive. Recent studies have predicted that, owing to the modification of phonon states in low-dimensional materials, the hydrodynamic phenomenon can occur at temperatures substantially higher than previously believed[113].

The interaction between elemental excitations, such as phonon–magnon coupling, in magnetic materials is another field that has attracted a lot of attention in recent years. Although the first attempts at studying such interactions by BLS date back to almost five decades ago in bulk YIG[117], interest has been re-ignited by the discovery of low-dimensional magnetic and antiferromagnetic materials[118,119]. BLS has been used for measuring the local temperature in studies related to spin caloritronics, where the interplay between the spin and heat transport is of interest[43,91]. It appears that the BLS technique could follow the same expansion-of-use trajectory as Raman spectroscopy and the Raman optothermal technique[119,120]. Recent examples of new BLS designs, for example, BLS systems with a resolution beyond the optical diffraction limit[81] and rotating microscopy, as well as the use of artificial-intelligence capabilities for probing samples with lateral dimensions below the micrometre scale, will elevate this photonic technique to an absolutely new level of capabilities.

Received: 11 November 2020; Accepted: 25 May 2021;
Published online: 22 July 2021

References

1. Brillouin, L. Diffusion de la lumière et des rayons X par un corps transparent homogène. Influence de l'agitation thermique. *Ann. Phys.* **17**, 88–122 (1922).
2. Mandelstam, L. Light scattering by inhomogeneous media. *Zh. Russ. Fiz. Khim. Ova.* **58**, 381 (1926).
3. Meng, Z., Traverso, A. J., Ballmann, C. W., Troyanova-Wood, M. A. & Yakovlev, V. V. Seeing cells in a new light: a renaissance of Brillouin spectroscopy. *Adv. Opt. Photonics* **8**, 300–327 (2016).
4. Raman, C. V. & Krishnan, K. S. A new type of secondary radiation. *Nature* **121**, 501–502 (1928).
5. Cardona, M. & Merlin, R. in *Light Scattering in Solids IX* Vol. 108 (eds Cardona, M. & Merlin, R.) Ch. 1 (Springer, 2006).
6. Fabelinskiĭ, I. L. The prediction and discovery of Rayleigh line fine structure. *Usp. Fiz. Nauk* **170**, 107–108 (2000).
7. Fabelinskiĭ, I. L. The discovery of combination scattering of light in Russia and India. *Phys. Usp.* **46**, 1105–1112 (2003).
8. Gross, E. Change of wave-length of light due to elastic waves at scattering in liquids. *Nature* **126**, 201–202 (1930).
9. Gross, E. The splitting of spectral lines at scattering of light by liquids. *Nature* **126**, 400 (1930).
10. Gross, E. über Änderung der WellenlÄnge bei Lichtzerstreuung in Kristallen. *Z. Phys.* **63**, 685–687 (1930).
11. Sandercock, J. R. in *Light Scattering in Solids III* Vol. 51 (eds Cardona, M. & Güntherodt, G.) 173–206 (Springer, 1982).
12. Scarponi, F. et al. High-performance versatile setup for simultaneous Brillouin–Raman microspectroscopy. *Phys. Rev. X* **7**, 031015 (2017).
13. Speziale, S., Marquardt, H. & Duffy, T. S. Brillouin scattering and its application in geosciences. *Rev. Mineral. Geochem.* **78**, 543–603 (2014).
14. Huang, C. Y. T. et al. Phononic and photonic properties of shape-engineered silicon nanoscale pillar arrays. *Nanotechnology* **31**, 30LT01 (2020).
15. Sledzinska, M. et al. 2D phononic crystals: progress and prospects in hypersound and thermal transport engineering. *Adv. Funct. Mater.* **30**, 1904434 (2019).
16. Graczykowski, B. et al. Phonon dispersion in hypersonic two-dimensional phononic crystal membranes. *Phys. Rev. B* **91**, 075414 (2015).
17. Yudistira, D. et al. Nanoscale pillar hypersonic surface phononic crystals. *Phys. Rev. B* **94**, 094304 (2016).
18. Rakhymzhanov, A. M. et al. Band structure of cavity-type hypersonic phononic crystals fabricated by femtosecond laser-induced two-photon polymerization. *Appl. Phys. Lett.* **108**, 201901 (2016).
19. Alonso-Redondo, E. et al. Phoxonic hybrid superlattice. *ACS Appl. Mater. Interfaces* **7**, 12488–12495 (2015).
20. Gomopoulos, N. et al. One-dimensional hypersonic phononic crystals. *Nano Lett.* **10**, 980–984 (2010).
21. Schneider, D. et al. Engineering the hypersonic phononic band gap of hybrid Bragg stacks. *Nano Lett.* **12**, 3101–3108 (2012).
22. Parsons, L. C. & Andrews, G. T. Off-axis phonon and photon propagation in porous silicon superlattices studied by Brillouin spectroscopy and optical reflectance. *J. Appl. Phys.* **116**, 033510 (2014).
23. Kargar, F. et al. Acoustic phonon dispersion engineering in bulk crystals via incorporation of dopant atoms. *Appl. Phys. Lett.* **112**, 191902 (2018).
24. Kargar, F. et al. Direct observation of confined acoustic phonon polarization branches in free-standing semiconductor nanowires. *Nat. Commun.* **7**, 13400 (2016).
25. Kuok, M. H., Lim, H. S., Ng, S. C., Liu, N. N. & Wang, Z. K. Brillouin study of the quantization of acoustic modes in nanospheres. *Phys. Rev. Lett.* **90**, 255502 (2003).
26. Cuffe, J. et al. Phonons in slow motion: dispersion relations in ultrathin Si membranes. *Nano Lett.* **12**, 3569–3573 (2012).
27. Graczykowski, B. et al. Elastic properties of few nanometers thick polycrystalline MoS_2 membranes: a nondestructive study. *Nano Lett.* **17**, 7647–7651 (2017).
28. Li, Y. et al. Brillouin study of acoustic phonon confinement in GeO_2 nanocubes. *Appl. Phys. Lett.* **91**, 093116 (2007).
29. Kargar, F. et al. Acoustic phonon spectrum and thermal transport in nanoporous alumina arrays. *Appl. Phys. Lett.* **107**, 171904 (2015).
30. Berrod, Q., Lagrené, K., Ollivier, J. & Zanotti, J.-M. Inelastic and quasi-elastic neutron scattering. Application to soft-matter. *EPJ Web Conf.* **188**, 05001 (2018).
31. Demokritov, S. O. et al. Bose–Einstein condensation of quasi-equilibrium magnons at room temperature under pumping. *Nature* **443**, 430–433 (2006).
32. Demidov, V. E. et al. Excitation of coherent propagating spin waves by pure spin currents. *Nat. Commun.* **7**, 10446 (2016).
33. Holanda, J., Maior, D. S., Azevedo, A. & Rezende, S. M. Detecting the phonon spin in magnon–phonon conversion experiments. *Nat. Phys.* **14**, 500–506 (2018).
34. Cho, J. et al. Thickness dependence of the interfacial Dzyaloshinskii–Moriya interaction in inversion symmetry broken systems. *Nat. Commun.* **6**, 7635 (2015).
35. Balinskiy, M., Kargar, F., Chiang, H., Balandin, A. A. & Khitun, A. G. Brillouin–Mandelstam spectroscopy of standing spin waves in a ferrite waveguide. *AIP Adv.* **8**, 056017 (2018).
36. Rumyantsev, S., Balinskiy, M., Kargar, F., Khitun, A. & Balandin, A. A. The discrete noise of magnons. *Appl. Phys. Lett.* **114**, 090601 (2019).

37. Eggleton, B. J., Poulton, C. G., Rakich, P. T., Steel, M. J. & Bahl, G. Brillouin integrated photonics. *Nat. Photonics* **13**, 664–677 (2019).
38. Zarifi, A. et al. Brillouin spectroscopy of a hybrid silicon-chalcogenide waveguide with geometrical variations. *Opt. Lett.* **43**, 3493–3496 (2018).
39. Boyd, R. W. *Nonlinear Optics* 4th edn (Elsevier, 2020).
40. Hayes, W. & Loudon, R. *Scattering of Light by Crystals* (Wiley, 1978).
41. Mutti, P. et al. in *Advances in Acoustic Microscopy* Vol. 1 (ed. Briggs, A.) 249–300 (Springer, 1995).
42. Bottani, C. E. & Fioretto, D. Brillouin scattering of phonons in complex materials. *Adv. Phys. X* **3**, 607–633 (2018).
43. Olsson, K. S., An, K. & Li, X. Magnon and phonon thermometry with inelastic light scattering. *J. Phys. D* **51**, 133001 (2018).
44. Loudon, R. Theory of surface-ripple Brillouin scattering by solids. *Phys. Rev. Lett.* **40**, 581–583 (1978).
45. Balandin, A. A. & Nika, D. L. Phononics in low-dimensional materials. *Mater. Today* **15**, 266–275 (2012).
46. Balandin, A. A. Phononics of graphene and related materials. *ACS Nano* **14**, 5170–5178 (2020).
47. Balandin, A. A. Thermal properties of graphene and nanostructured carbon materials. *Nat. Mater.* **10**, 569–581 (2011).
48. Xiao, Y., Chen, Q., Ma, D., Yang, N. & Hao, Q. Phonon transport within periodic porous structures—from classical phonon size effects to wave effects. *ES Mater. Manuf.* **5**, 2–18 (2019).
49. Hussein, M. I., Tsai, C. & Honarvar, H. Thermal conductivity reduction in a nanophononic metamaterial versus a nanophononic crystal: a review and comparative analysis. *Adv. Funct. Mater.* **30**, 1906718 (2020).
50. Djafari-Rouhani, B., El-Jallal, S. & Pennec, Y. Phoxonic crystals and cavity optomechanics. *C. R. Phys.* **17**, 555–564 (2016).
51. Johnson, W. L. et al. Vibrational modes of GaN nanowires in the gigahertz range. *Nanotechnology* **23**, 495709 (2012).
52. Still, T. et al. The 'music' of core–shell spheres and hollow capsules: influence of the architecture on the mechanical properties at the nanoscale. *Nano Lett.* **8**, 3194–3199 (2008).
53. Sun, J. Y. et al. Hypersonic vibrations of Ag@SiO_2 (cubic core)–shell nanospheres. *ACS Nano* **4**, 7692–7698 (2010).
54. Balandin, A. & Wang, K. L. Significant decrease of the lattice thermal conductivity due to phonon confinement in a free-standing semiconductor quantum well. *Phys. Rev. B* **58**, 1544–1549 (1998).
55. Pokatilov, E. P., Nika, D. L. & Balandin, A. A. Confined electron-confined phonon scattering rates in wurtzite AlN/GaN/AlN heterostructures. *J. Appl. Phys.* **95**, 5626–5632 (2004).
56. Duval, E. Far-infrared and Raman vibrational transitions of a solid sphere: selection rules. *Phys. Rev. B* **46**, 5795–5797 (1992).
57. Dainese, P. et al. Stimulated Brillouin scattering from multi-GHz-guided acoustic phonons in nanostructured photonic crystal fibres. *Nat. Phys.* **2**, 388–392 (2006).
58. Pennec, Y. et al. Sensing light and sound velocities of fluids in 2D phoxonic crystal slab. In *Proc. IEEE Sensors* 355–357 (IEEE, 2014).
59. Eichenfield, M., Chan, J., Camacho, R. M., Vahala, K. J. & Painter, O. Optomechanical crystals. *Nature* **462**, 78–82 (2009).
60. Garín, M., Solà, M., Julian, A. & Ortega, P. Enabling silicon-on-silicon photonics with pedestalled Mie resonators. *Nanoscale* **10**, 14406–14413 (2018).
61. Sebastian, T., Schultheiss, K., Obry, B., Hillebrands, B. & Schultheiss, H. Micro-focused Brillouin light scattering: imaging spin waves at the nanoscale. *Front. Phys.* **3**, 35 (2015).
62. Madami, M., Gubbiotti, G., Tacchi, S., Carlotti, G. & Stamps, R. L. Application of microfocused Brillouin light scattering to the study of spin waves in low-dimensional magnetic systems. *Solid State Phys.* **63**, 79–150 (2012).
63. Cottam, M. G. & Lockwood, D. J. *Light Scattering in Magnetic Solids* (Wiley, 1986).
64. Rezende, S. M. *Fundamentals of Magnonics* Vol. 969 (Springer, 2020)
65. Fleury, P. A. & Loudon, R. Scattering of light by one- and two-magnon excitations. *Phys. Rev.* **166**, 514–530 (1968).
66. Demidov, V. E. & Demokritov, S. O. Magnonic waveguides studied by microfocus brillouin light scattering. *IEEE Trans. Magn.* **51**, 0800215 (2015).
67. Demokritov, S. O., Hillebrands, B. & Slavin, A. N. Brillouin light scattering studies of confined spin waves: linear and nonlinear confinement. *Phys. Rep.* **348**, 441–489 (2001).
68. Serga, A. A., Schneider, T., Hillebrands, B., Demokritov, S. O. & Kostylev, M. P. Phase-sensitive Brillouin light scattering spectroscopy from spin-wave packets. *Appl. Phys. Lett.* **89**, 063506 (2006).
69. Vogt, K. et al. All-optical detection of phase fronts of propagating spin waves in a $Ni_{81}Fe_{19}$ microstripe. *Appl. Phys. Lett.* **95**, 182508 (2009).
70. Pirro, P. et al. Interference of coherent spin waves in micron-sized ferromagnetic waveguides. *Phys. Status Solidi B* **248**, 2404–2408 (2011).
71. Vogt, K. et al. Spin waves turning a corner. *Appl. Phys. Lett.* **101**, 042410 (2012).
72. Vogt, K. et al. Realization of a spin-wave multiplexer. *Nat. Commun.* **5**, 3727 (2014).
73. Borisenko, I. V. et al. Direct evidence of spatial stability of Bose-Einstein condensate of magnons. *Nat. Commun.* **11**, 1691 (2020).
74. Nembach, H. T., Shaw, J. M., Weiler, M., Jué, E. & Silva, T. J. Linear relation between Heisenberg exchange and interfacial Dzyaloshinskii–Moriya interaction in metal films. *Nat. Phys.* **11**, 825–829 (2015).
75. Ma, X. et al. Interfacial Dzyaloshinskii-Moriya interaction: effect of 5d band filling and correlation with spin mixing conductance. *Phys. Rev. Lett.* **120**, 157204 (2018).
76. Benguettat-El Mokhtari, I. et al. Interfacial Dzyaloshinskii-Moriya interaction, interface-induced damping and perpendicular magnetic anisotropy in Pt/Co/W based multilayers. *J. Appl. Phys.* **126**, 133902 (2019).
77. Bouloussa, H. et al. Dzyaloshinskii-Moriya interaction induced asymmetry in dispersion of magnonic Bloch modes. *Phys. Rev. B* **102**, 014412 (2020).
78. Stashkevich, A. A., Djemia, P., Fetisov, Y. K., Bizière, N. & Fermon, C. High-intensity Brillouin light scattering by spin waves in a permalloy film under microwave resonance pumping. *J. Appl. Phys.* **102**, 103905 (2007).
79. Demidov, V. E. et al. Generation of the second harmonic by spin waves propagating in microscopic stripes. *Phys. Rev. B* **83**, 054408 (2011).
80. Demidov, V. E. et al. Nonlinear propagation of spin waves in microscopic magnetic stripes. *Phys. Rev. Lett.* **102**, 177207 (2009).
81. Jersch, J. et al. Mapping of localized spin-wave excitations by near-field Brillouin light scattering. *Appl. Phys. Lett.* **97**, 152502 (2010).
82. Rezende, S. M. Theory of coherence in Bose–Einstein condensation phenomena in a microwave-driven interacting magnon gas. *Phys. Rev. B* **79**, 174411 (2009).
83. Rüegg, C. et al. Bose–Einstein condensation of the triplet states in the magnetic insulator $TlCuCl_3$. *Nature* **423**, 62–65 (2003).
84. Demidov, V. E., Dzyapko, O., Demokritov, S. O., Melkov, G. A. & Slavin, A. N. Observation of spontaneous coherence in Bose–Einstein condensate of magnons. *Phys. Rev. Lett.* **100**, 047205 (2008).
85. Tupitsyn, I. S., Stamp, P. C. E. & Burin, A. L. Stability of Bose–Einstein condensates of hot magnons in yttrium iron garnet films. *Phys. Rev. Lett.* **100**, 257202 (2008).
86. Gubbiotti, G. et al. Finite size effects in patterned magnetic permalloy films. *J. Appl. Phys.* **87**, 5633–5635 (2000).
87. Roussigné, Y., Chérif, S. M., Dugautier, C. & Moch, P. Experimental and theoretical study of quantized spin-wave modes in micrometer-size permalloy wires. *Phys. Rev. B* **63**, 134429 (2001).
88. Chérif, S. M., Roussigné, Y. E. & Moch, P. Finite-size effects in arrays of permalloy square dots. *IEEE Trans. Magn.* **38**, 2529–2531 (2002).
89. Gubbiotti, G. et al. Magnetostatic interaction in arrays of nanometric permalloy wires: a magneto-optic Kerr effect and a Brillouin light scattering study. *Phys. Rev. B* **72**, 224413 (2005).
90. Kargar, F. et al. Brillouin–Mandelstam spectroscopy of stress-modulated spatially confined spin waves in Ni thin films on piezoelectric substrates. *J. Magn. Magn. Mater.* **501**, 166440 (2020).
91. Birt, D. R. et al. Brillouin light scattering spectra as local temperature sensors for thermal magnons and acoustic phonons. *Appl. Phys. Lett.* **102**, 082401 (2013).
92. Gubbiotti, G. et al. Brillouin light scattering studies of planar metallic magnonic crystals. *J. Phys. D* **43**, 264003 (2010).
93. Bailey, M. et al. Viscoelastic properties of biopolymer hydrogels determined by Brillouin spectroscopy: a probe of tissue micromechanics. *Sci. Adv.* **6**, eabc1937 (2020).
94. Graczykowski, B., Vogel, N., Bley, K., Butt, H.-J. & Fytas, G. Multiband hypersound filtering in two-dimensional colloidal crystals: adhesion, resonances, and periodicity. *Nano Lett.* **20**, 1883–1889 (2020).
95. Hesami, M. et al. Elastic wave propagation in smooth and wrinkled stratified polymer films. *Nanotechnology* **30**, 045709 (2019).
96. Graczykowski, B., Gueddida, A., Djafari-Rouhani, B., Butt, H.-J. & Fytas, G. Brillouin light scattering under one-dimensional confinement: symmetry and interference self-canceling. *Phys. Rev. B* **99**, 165431 (2019).
97. Alonso-Redondo, E. et al. Robustness of elastic properties in polymer nanocomposite films examined over the full volume fraction range. *Sci Rep.* **8**, 16986 (2018).
98. Sato, A. et al. Cavity-type hypersonic phononic crystals. *New J. Phys.* **14**, 113032 (2012).
99. Koski, K. J., Akhenblit, P., McKiernan, K. & Yarger, J. L. Non-invasive determination of the complete elastic moduli of spider silks. *Nat. Mater.* **12**, 262–267 (2013).
100. Scarcelli, G. et al. Noncontact three-dimensional mapping of intracellular hydromechanical properties by Brillouin microscopy. *Nat. Methods* **12**, 1132–1134 (2015).
101. Wu, P. J. et al. Water content, not stiffness, dominates Brillouin spectroscopy measurements in hydrated materials. *Nat. Methods* **15**, 561–562 (2018).

102. Prevedel, R., Diz-Muñoz, A., Ruocco, G. & Antonacci, G. Brillouin microscopy: an emerging tool for mechanobiology. *Nat. Methods* **16**, 969–977 (2019).
103. So, P. Brillouin bioimaging. *Nat. Photonics* **2**, 13–14 (2008).
104. Scarcelli, G. & Yun, S. H. Confocal Brillouin microscopy for three-dimensional mechanical imaging. *Nat. Photonics* **2**, 39–43 (2008).
105. Pérez-Cota, F. et al. High resolution 3D imaging of living cells with sub-optical wavelength phonons. *Sci Rep.* **6**, 39326 (2016).
106. Wang, P., Lu, L. & Bertoldi, K. Topological phononic crystals with one-way elastic edge waves. *Phys. Rev. Lett.* **115**, 104302 (2015).
107. Yang, Z. et al. Topological acoustics. *Phys. Rev. Lett.* **114**, 114301 (2015).
108. Mousavi, S. H., Khanikaev, A. B. & Wang, Z. Topologically protected elastic waves in phononic metamaterials. *Nat. Commun.* **6**, 8682 (2015).
109. He, C. et al. Acoustic topological insulator and robust one-way sound transport. *Nat. Phys.* **12**, 1124–1129 (2016).
110. Zhu, H. et al. Observation of chiral phonons. *Science* **359**, 579–582 (2018).
111. Chen, H., Zhang, W., Niu, Q. & Zhang, L. Chiral phonons in two-dimensional materials. *2D Mater.* **6**, 012002 (2019).
112. Griffin, A. Brillouin light scattering from crystals in the hydrodynamic region. *Rev. Mod. Phys.* **40**, 167–205 (1968).
113. Huberman, S. et al. Observation of second sound in graphite at temperatures above 100 K. *Science* **364**, 375–379 (2019).
114. Lee, S. & Li, X. in *Nanoscale Energy Transport* (ed. Liao, B.) Ch. 1 (IOP, 2020).
115. Aytan, E. et al. Spin–phonon coupling in antiferromagnetic nickel oxide. *Appl. Phys. Lett.* **111**, 252402 (2017).
116. An, K. et al. Magnons and phonons optically driven out of local equilibrium in a magnetic insulator. *Phys. Rev. Lett.* **117**, 107202 (2016).
117. Sandercock, J. R. & Wettling, W. Light scattering from thermal acoustic magnons in yttrium iron garnet. *Solid State Commun.* **13**, 1729–1732 (1973).
118. Burch, K. S., Mandrus, D. & Park, J. G. Magnetism in two-dimensional van der Waals materials. *Nature* **563**, 47–52 (2018).
119. Kargar, F. et al. Phonon and thermal properties of quasi-two-dimensional $FePS_3$ and $MnPS_3$ antiferromagnetic semiconductors. *ACS Nano* **14**, 2424–2435 (2020).
120. Balandin, A. A. et al. Superior thermal conductivity of single-layer graphene. *Nano Lett.* **8**, 902–907 (2008).

Acknowledgements

We acknowledge the support of the National Science Foundation (NSF) via a Major Research Instrumentation (MRI) project DMR 2019056 entitled 'Development of a Cryogenic Integrated Micro-Raman-Brillouin-Mandelstam Spectrometer'. A.A.B. also acknowledges the support of the Designing Materials to Revolutionize and Engineer our Future (DMREF) program via a project DMR-1921958 entitled 'Collaborative research: data driven discovery of synthesis pathways and distinguishing electronic phenomena of 1D van der Waals bonded solids', and the support of the US Department of Energy (DOE) via a project DE-SC0021020 entitled 'Physical mechanisms and electric-bias control of phase transitions in quasi-2D charge-density-wave quantum materials'. We thank M. Kargar and Z. Barani for their help with the preparation of schematics in Figs. 1e and 3a.

Competing interests

The authors declare no competing interests.

Additional information

Correspondence should be addressed to F.K.

Peer review information *Nature Photonics* thanks Sergej Demokritov, Benjamin Eggleton and the other, anonymous, reviewer(s) for their contribution to the peer review of this work.